Titanium diboride nanopowders: New horizons for the enhancement of *in vitro* bioactivity and bone regeneration

Chuang Qian^{a,#}, Peiwei Yang^{b,#}, Lihong He^c and Meixiong Zhan^{d,*}

Bone regeneration is a critical focus in biomedical research, necessitating materials that enhance osteogenesis and integrate well with bone tissue. This study investigates titanium diboride (TiB₂) nanopowders synthesized through mechanical attrition, assessing their microstructural properties and *in vitro* bioactivity in simulated body fluid (SBF). X-ray diffraction (XRD) analysis revealed distinct phase compositions influenced by varying magnesium (Mg) and aluminum (Al) contents in the precursor materials, with only TiB₂ remaining post-leaching in the 100% Mg system. Field-emission scanning electron microscopy (FESEM) images indicated that the 100% Mg system exhibited a homogeneous microstructure with flower-like TiB₂ structures, while the mixed systems showed significant agglomeration. *In vitro* bioactivity tests demonstrated that the TiB₂ in the pure Mg system formed a thicker apatite layer compared to the systems containing Al, suggesting enhanced bioactivity likely due to improved ionic interactions and surface reactivity. This study provides foundational insights into TiB₂'s potential as a novel material for orthopedic applications.

Keywords: Biomaterials, TiB2, Mechanical attrition, Phase transformation, Bioactivity.

Introduction

Bone regeneration remains a crucial area in biomedical research, driven by the need for materials that can integrate seamlessly with bone tissue while promoting osteogenesis [1]. Among ceramic-based materials, titanium diboride (TiB₂), a ceramic material known for its exceptional hardness, high melting point, and stability, has recently gained attention for its potential in bone regeneration applications [2, 3]. Traditionally studied for applications in cutting tools and protective coatings, TiB2 has recently emerged as a promising candidate for biomedical applications, particularly in orthopedic coatings, owing to its biocompatibility and chemical inertness [4, 5]. Several studies have reported the effective use of ceramic nanopowders in promoting osteointegration and mechanical reinforcement of implant surfaces [6, 7], including recent efforts in the development of boride- and nitride-based systems with bioactive characteristics [8].

*Corresponding author: Tel: +86 18370291626 Fax: +86 18370291626

E-mail: zhan198706@outlook.com

Despite these advances, the potential of TiB₂, especially in nanopowder form, for bone regenerative applications remains largely underexplored. To address this gap, this study investigates nanostructured TiB₂ powders synthesized via high-energy mechanical attrition, a top-down ball milling technique widely applied in the fabrication of fine-grained ceramic materials with enhanced surface activity and tailored morphology [9]. The process allows for structural refinement and particle size control [10, 11], factors known to influence cellular adhesion, protein adsorption, and *in vitro* mineralization [12].

By assessing the microstructural properties and calcium phosphate deposition behavior of TiB₂ nanopowders, this work seeks to establish their feasibility as a next-generation material for bone regeneration. This research contributes foundational insights into the use of TiB₂ in orthopedic coatings, providing a new direction for advanced bone regeneration strategies.

Materials and Methods

The following reagents were used as received, without further purification: titanium dioxide (TiO_2 , 99% purity), boron oxide (B_2O_3 , 99.95% purity), magnesium (Mg,

^aDepartment of Orthopedics, Children's Hospital of Fudan University, National Children's Medical Center, Shanghai, 201102, China

^bDepartment of Orthopedics, The 910th Hospital of the Chinese People's Liberation Army Joint Logistic Support Force, Quanzhou, Fujian, 362000, China

^cDepartment of General Practice, The General Hospital of Western Theater Command of Chinese People's Liberation Army, Chengdu, Sichuan, 610000, China

^dDepartment of Orthopedics, Jiujiang Hospital of Traditional Chinese Medicine, Jiujiang, Jiangxi, 332000, China

^{*}These authors contributed equally to this work.

Table 1. DOE for the synthesis of nanosized TiB₂.

Run	Ball-to-Powder Ratio	Rotation Speed	Ball Size	TiB ₂ Phase Purity	Observations
	(BPR)	(rpm)	(mm)	(%)	
1	5:1	450	10	75	Coarse particles observed
2	5:1	550	20	78	Coarse particles observed
3	5:1	650	30	76	Coarse particles observed
4	10:1	450	10	82	Moderate particle size
5	10:1	550	20	90	Uniform particle size, high purity
6	10:1	650	30	85	Slightly larger particles
7	15:1	450	10	80	Uneven particle size
8	15:1	550	20	84	Uniform particles
9	15:1	650	30	79	Coarse particles

>97% purity), and aluminum (Al, 99.7% purity). All chemicals were sourced from Merck and were selected based on their high purity levels to ensure consistent reaction outcomes. Nanosized TiB2 was synthesized via mechanical attrition using a high-energy planetary mill equipped with hardened chromium steel vials (125 mL). The milling process was conducted under optimized conditions identified through a design of experiments (DOE) approach (Table 1), which established a ball-topowder ratio (BPR) of 10:1, a rotation speed of 550 rpm, and the use of 20 mm balls to enhance phase purity. A three-factor, three-level factorial design was implemented to investigate the effects of milling parameters on the synthesis of nanosized TiB2-based nanocomposites. The parameters included ball-to-powder ratio (BPR), rotation speed, and ball size. The following table summarizes the experimental conditions and the corresponding outcomes for phase purity, as assessed by XRD.

To prevent oxidation during milling, the vials were purged and filled with high-purity argon gas. Following the milling process, the powders underwent a standard leaching procedure using a 10% HCl solution at 60 °C for 1 h to effectively remove undesirable phases. The phase purity and crystallographic properties of the synthesized powders were evaluated using X-ray diffraction (XRD; Philips, Cu-K α radiation) over a 2θ range of 10° to 90°. The morphological features of the specimens were examined using field-emission scanning electron microscopy (FESEM; CARL ZEISS-AURIGA 60) and field-emission scanning transmission electron microscopy (FE-STEM; Hitachi S-4700), complemented by energy-dispersive X-ray spectroscopy (EDS) for elemental composition verification. Bioactivity tests in vitro were performed by following the well-known protocol proposed by Kokubo in order to investigate the bioactive properties of the material. Samples were immersed in simulated body fluid-a solution that mimics the ion concentration of human blood plasma-under physiological conditions. The samples were submerged for 21 days, during which the surface morphology, chemical composition, and hydroxyapatite

formation were periodically evaluated as an indication of bioactivity. This method is known to be one of the standard techniques for *in vitro* testing of the ability of materials to form a bond with bone-like tissue in conditions mimicking those *in vivo* [13].

Results and Discussion

Fig. 1 presents the Rietveld refinement XRD profiles of TiB2-based systems both before and after leaching, including systems 1 (100% Mg), 2 (75 wt% Mg-25 wt% Al), and 3 (50 wt% Mg-50 wt% Al). The figure also includes schematic representations of the crystal structures and phase transformations observed across the multiphase compositions of these systems. XRD profiles for each system obtained through the Rietveld refinement gave a detailed insight into the phase composition, which has clearly been changed by varying the Mg and Al contents after the milling and leaching processes. XRD analysis after milling in system 1 (with 100% Mg) showed the presence of TiB₂ (with reference code #cod 2002799), Mg₂TiO₄ (reference code #cod 9013398), and MgO (reference code #04-010-4039) phases (Fig. However, after leaching, it detected only the TiB₂ phase, which indicates that the dissolution and removal of MgO and Mg₂TiO₄ phases were carried out effectively, leaving TiB₂ as the major phase (Fig. 1a'). That would mean the milling and leaching conditions effectively removed the unwanted MgO and Mg2TiO4 phases, leaving only TiB₂ as a phase stable under the current conditions. On the other hand, system 2 contained 75 wt% Mg and 25 wt% Al. After milling, the following phases were present in the XRD profile: TiB2, Mg2TiO4, MgAl2O4 (reference code #cod 9002059), and MgO (Fig. 1b). After leaching, the major phases remained as TiB2 and MgAl₂O₄, while MgO and Mg₂TiO₄ phases were largely removed, which shows the selective stability of TiB2 and MgAl₂O₄ in the leached system (Fig. 1b'). In system 3, with 50 wt% Mg and 50 wt% Al, the phase composition after milling as well as after leaching was the same as for System 2, but the relative proportion of the phases had

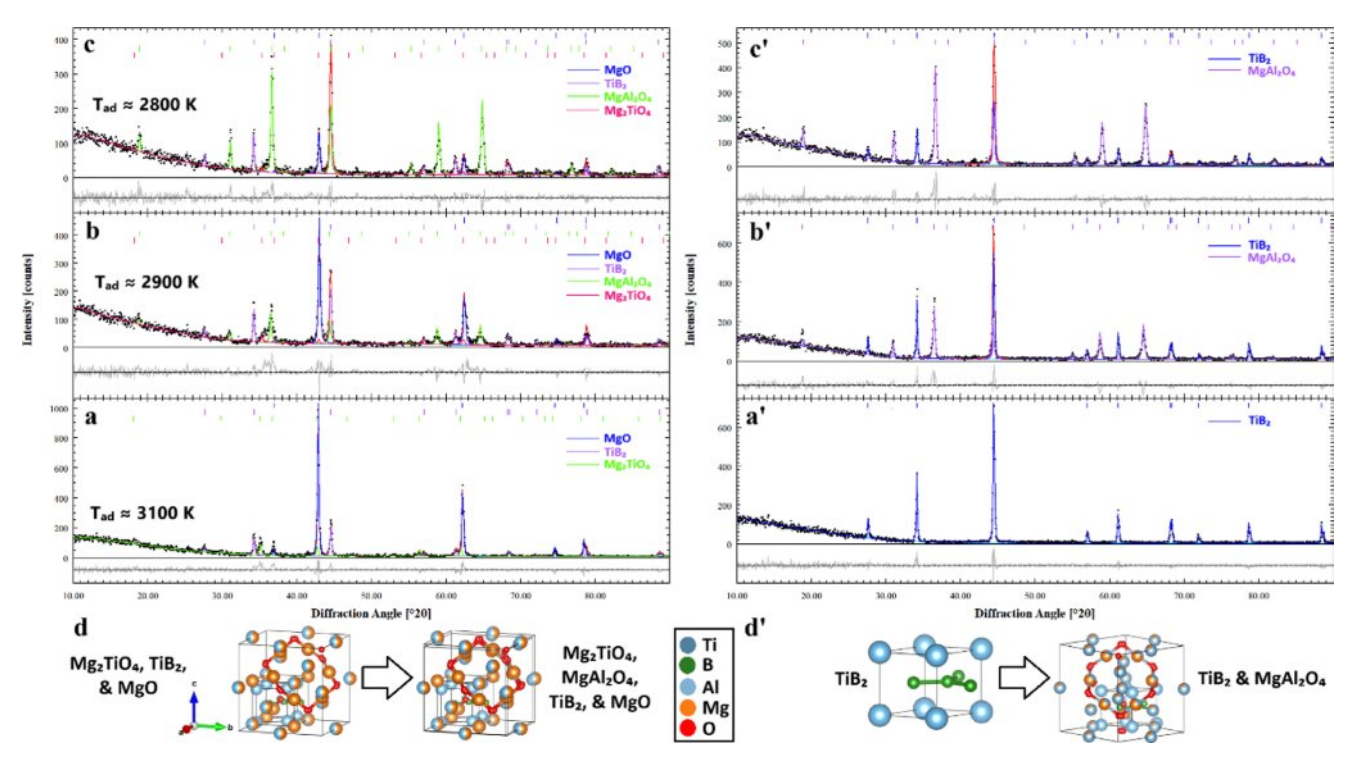


Fig. 1. Rietveld refinement XRD profiles of TiB₂-based systems before and after leaching: (a, a') System 1 (100% Mg), (b, b') System 2 (75 wt% Mg–25 wt% Al), and (c, c') System 3 (50 wt% Mg–50 wt% Al) as well as schematic representations of crystal structures and phase transformations of multiphase compositions across the systems. TiB₂ (#cod_2002799), Mg₂TiO₄ (#cod_9013398), MgAl₂O₄ (#cod_9002059), and MgO (#04-010-4039).

apparently shifted (Fig. 1c and c'). Correspondingly, with the increase of Al content in system 3, the proportion of TiB₂ decreased from 35.18 \pm 1.05% in system 2 to 19.68 \pm 0.97% in system 3, while the Mg₂TiO₄ phase increased correspondingly from 64.82 \pm 1.05% to 80.32 \pm 0.97%, which indicates that higher Al content favors the stabilization of Mg₂TiO₄ rather than TiB₂ after the leaching process.

These changes in phase composition are further supported by the estimated adiabatic temperatures of the systems. Accordingly, the highest adiabatic temperature of about 3100 K in system 1 was for a pure Mg composition and would thus correspond to the highest exothermic reaction upon milling. Systems 2 and 3, however, with their Mg contents progressively reduced, had lower adiabatic temperatures of about 2900 K and 2800 K, respectively, indicating more moderated exothermic reactions. This trend underlines the influence of Mg and Al contents in view of phase stability as well as thermal behavior of these systems, since a decrease in the Mg content results in the lowering of the overall exothermic reaction temperatures [14]. The crystal structures and phase changes have also been represented in schematic forms showing the evolution of multi-phase compositions across systems (in Fig. 1d and d'). These diagrams represent structural changes involved with mechanical milling and leaching processes, whereby different phases will form, dissolve, or stabilize depending on the Mg and Al content in each system: TiB₂, MgO, Mg₂TiO₄, and MgAl₂O₄. These phase transformations put into perspective the evolution of the composition of the material at an atomic level that reflects the interaction among the different phases and how these phases retain and dissolve due to the leaching process [15].

Fig. 2 provides insights into the microstructural characteristics and elemental composition of the leached products from systems 1, 2, and 3. Figs. 2a-c display FESEM images, highlighting that system 1 exhibits a homogeneous microstructure with flower-like TiB₂ structures averaging around 300 ± 20 nm in diameter. In contrast, systems 2 and 3 demonstrate significant agglomeration resulting from milling and subsequent leaching [16], with coarse clusters comprising multiple fine particles. Notably, system 3, characterized by the lowest Mg content and highest Al content, reveals not only these clusters but also the presence of larger platelike particles. These larger particles are likely attributed to the increased volume fraction of the spinel phase (MgAl₂O₄) within the system [17]. Furthermore, the FE-STEM image shown in Fig. 2d reveals a nanosized flow-like TiB2 structure, corroborating the observations from the FESEM image of TiB2. The accompanying EDS analysis further verifies the presence of both TiB2 and MgAl₂O₄ phases (Fig. 2e). Here, the non-detection of boron in EDS analysis is likely due to the limitations in detecting light elements, detector resolution issues,

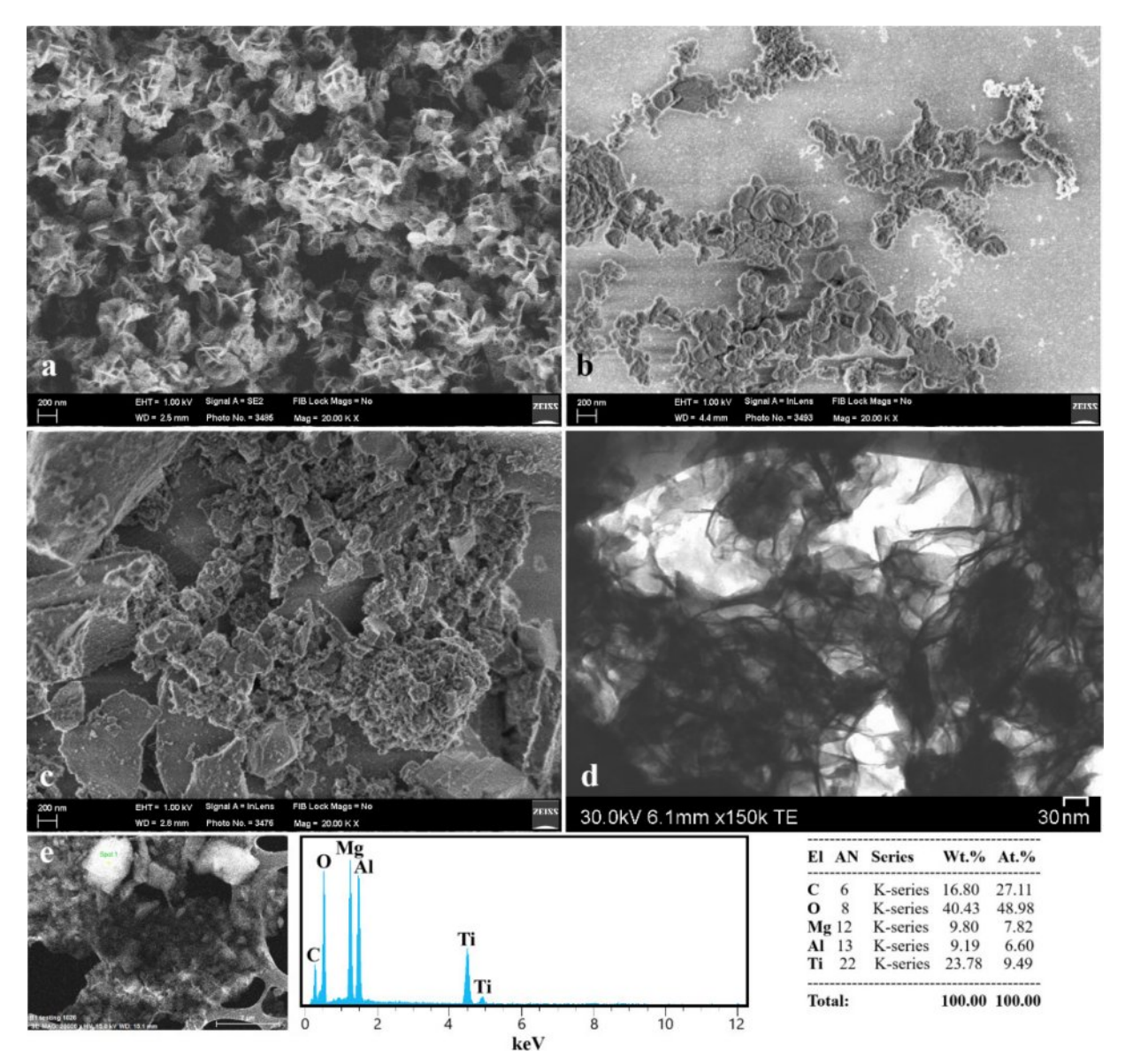


Fig. 2. Microstructural and compositional analysis of leached products: FESEM images of (a) System 1, (b) System 2, and (c) System 3 as well as (d) FE-STEM image of single-phase TiB₂ after leaching of System 1 and (e) EDS analysis of system 3 after leaching.

sample thickness, beam intensity, interference, and high counting rates. To ensure reproducibility, all microstructural and elemental analyses were conducted on three independently prepared samples per system (n = 3), and consistent trends were observed across replicates.

Fig. 3 illustrates the *in vitro* bioactivity of the leached samples immersed in SBF for 21 days, reflecting the formation of bone-like apatite layers on the surface of each system. In Fig. 3a, FESEM has shown the development of an apatite layer on system 1 that consists only of a single-phase TiB₂. The present layer is well-defined and dense, reflecting the good bioactive behavior. Fig. 3b presents the apatite layer formed on system 2; this layer is less homogeneous than in the previous case, probably because the presence of a second phase changes the reactivity of the surface and, therefore,

its interaction with SBF.

The enhanced bioactivity is further reflected in system 1, in the *in vitro* thicker and better-formed apatite layer compared to system 2. This enhancement in bioactivity can be justified in light of the increased surface reactivity of TiB₂, favoring effective ionic interactions and a strong apatite layer in SBF. The higher surface energy and greater availability of reactive sites on TiB₂ may thus explain its higher ability to interact with the ions in the SBF to form a thicker apatite layer when compared to the composite of TiB₂/MgAl₂O₄ in system 2 [18]. Fig. 3c shows the EDS spectrum from system 1, gives further support to this observation with a Ca/P ratio of around 2.02 ± 0.06 . This ratio agrees with the formation of either calcium-deficient or calcium-rich apatite phases, such as calcium-rich carbonate apatite and other nonstoichiometric apatite

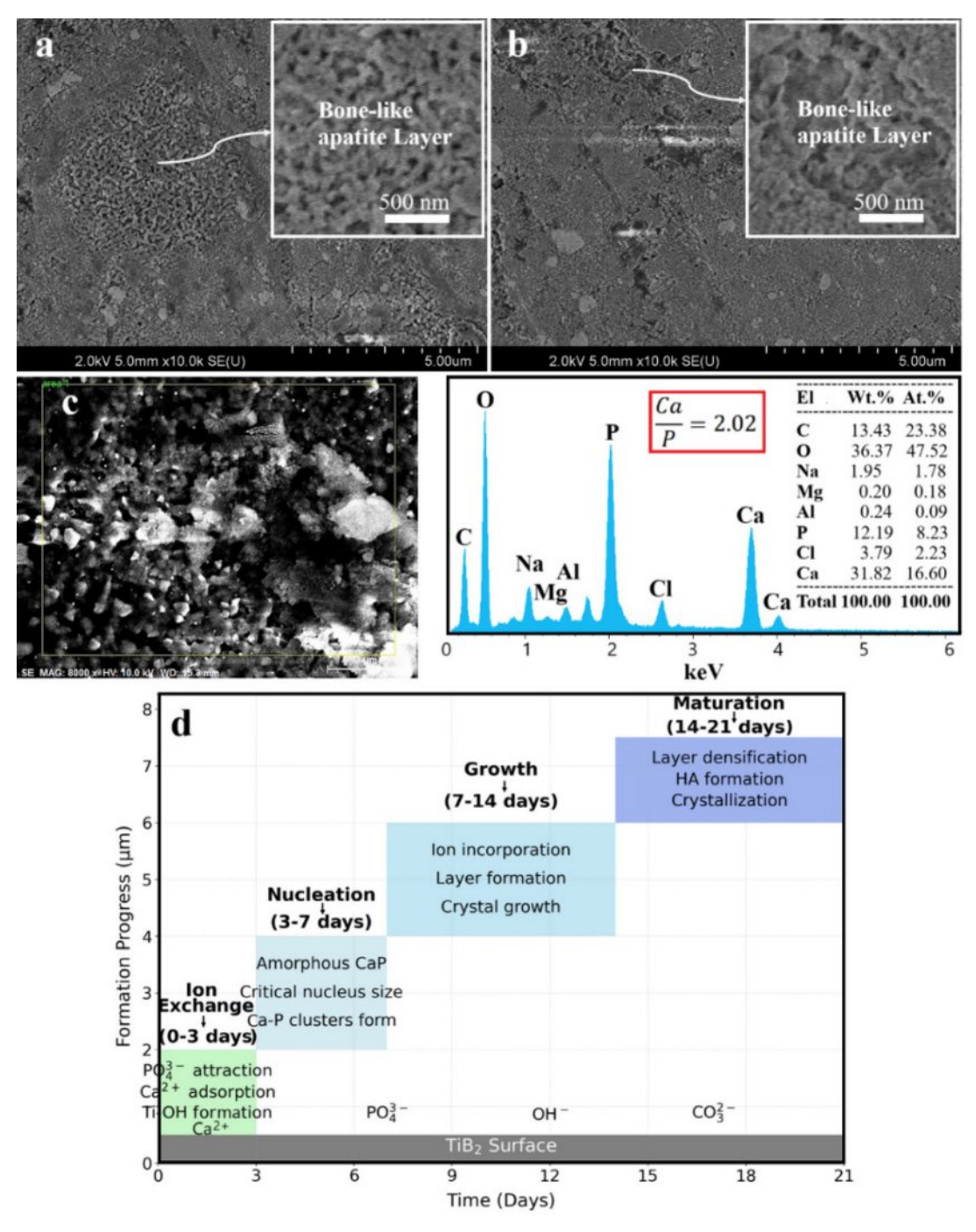


Fig. 3. In vitro bioactivity of the leached samples immersed in SBF for 21 days, (a, c) System 1 and (b) System 2, as well as (d) mechanism of bone-like apatite formation.

forms known to form under conditions simulating bone mineralization *in vivo* [19]. This result points to the fact that the apatite layer formed on system 1 is chemically similar to those present in natural bone tissue; hence, the material will be more biologically active. It should be noted that to improve clarity and transparency, the immersion experiments were performed in triplicate (n = 3), and average Ca/P ratios and morphological features were consistently reproduced. In addition, although specific surface area measurements (e.g., BET

analysis) were not conducted in this study, the improved bioactivity of system 1 is inferred from the consistent nanoscale morphology, increased surface energy, and Ca/P ratio analysis. Future work will include quantitative porosity and surface area analyses to further validate this correlation. Besides, the flower-like surface morphology of TiB₂ nanoparticles, as observed in FESEM and FESTEM images, may play a critical role in promoting osseointegration. Such nanoscale features can enhance protein adsorption and provide favorable topographical

cues for osteoblast attachment, proliferation, and extracellular matrix deposition—key processes in early bone bonding [20].

To contextualize the bioactivity of TiB2, it is worth noting that while materials such as TiO2 and HA are widely used in orthopedic applications for their wellestablished bioactive properties [21], TiB2 offers a unique combination of structural stability, chemical inertness, and bioactive surface potential [22]. Compared to TiO₂, which promotes apatite nucleation primarily via surface HA, TiB₂ may enable stronger ionic interactions due to its higher surface energy and fine particle morphology [21, 23]. Although HA exhibits excellent biological affinity due to its chemical similarity to bone mineral, it lacks the mechanical robustness of TiB2. Therefore, TiB₂ nanopowders present a promising balance between mechanical performance and in vitro bioactivity, especially when surface-engineered or nanostructured to enhance apatite formation.

Fig. 3d describes a schematic process responsible for bone-like apatite formation on TiB2: the interaction of TiB₂ with SBF first occurs by exchanging solution ions with those on the surface of the material. This forms the modified surface, which is favorable for the nucleation of the apatite crystals. As these ions further interact, the growing apatite layer grows and matures into a dense, bone-like apatite layer on the surface of TiB2. The graph included in Fig. 3d is intended as a conceptual illustration based on known apatite formation mechanisms from literature and our qualitative observations. It is not derived from direct thickness measurements but rather outlines the theoretical progression of apatite development over a 21-day immersion period. This process consists of four stages: Ion Exchange (0-3 days), during which PO₄³⁻ ions attract, Ca2+ ions adsorb, and the formation of Ti-OH groups leads to the advancement of formation from 0 to 3 µm [24]; Nucleation (3-7 days), during which Ca-P clusters form, attain a critical nucleus size, and then form amorphous CaP, while the formation progress advances to 5 µm [25]; Growth (7-14 days), during which incorporation of ions and crystal growth lead to the building of a thicker and more stable layer, while the formation progress advances from 5 to 6 µm [26]; and Maturation (14-21 days), during which densification and the formation of HA lead to crystallization, while the formation progress reaches 6 to 7 µm [27].

These findings, combined with all the others, underlined that the phase composition of the system plays a great role in influencing the bioactivity concerning apatite layer formation. Results emphasize the decisive role of both material composition and surface properties with regard to material fate in clinical applications [28]. The present study is focused on the fundamental *in vitro* bioactivity assessment of TiB₂ powders through SBF immersion, as an initial step toward orthopedic applicability. While no cytotoxicity assays were conducted at this stage, future work will include MTT and live/dead assays

to comprehensively evaluate cellular responses and biocompatibility.

Conclusions

The findings of this research highlight the potential of TiB₂ nanopowders synthesized via mechanical attrition as a promising material for bone regeneration. The key conclusion derived is that the appropriate milling and subsequent leaching processes have effectively removed the unwanted phases, leaving TiB2 as the major stable phase in system 1 (100% Mg). In system 2 (75 wt% Mg-25 wt% Al), the phases which remained after leaching were TiB2 and MgAl2O4, indicating their selective stability. In system 3 (50 wt% Mg-50 wt% Al), the increased Al content favors the stabilization of Mg₂TiO₄ over TiB₂, demonstrating that phase composition and stability can vary with changing Al content. The microstructural features of the 100% Mg system were marked by homogeneous, flower-like TiB2 structures averaging approximately 300 nm in diameter, which contributed to the enhanced in vitro bioactivity. This was further supported by the formation of a thicker apatite layer, a clear indication of the material's superior bioactive performance. The distinct phase compositions observed in the varying Mg and Al systems emphasize the influence of elemental ratios on bioactivity and phase stability. Moreover, the successful synthesis and characterization of TiB2 nanopowders pave the way for future studies focused on their application in orthopedic coatings, where mechanical robustness and biocompatibility are crucial. Overall, this research offers valuable insights into advanced materials for bone regeneration strategies, promoting further exploration in this vital area of biomedical engineering.

References

- M. Hao, L. Xue, X. Wen, L. Sun, L. Zhang, K. Xing, X. Hu, J. Xu, and D. Xing, Acta Biomater. 183 (2024) 1-29.
- Ö. Varlık, Y. Göncü, and A. Nuran, Mater. Chem. Phys. 282 (2022) 125927.
- 3. A.M.A. Aljafery, A.A. Fatalla, and J. Haider, J. Biomed. Mater. Res. B: Appl. Biomater. 112 (2024) e35490.
- 4. S. Das, in, 2014.
- A. Kumawat, K. Jasuja, and C. Ghoroi, ACS Appl. Bio Mater. 6 (2023) 4111-4126.
- B. Mehdikhani, and G.H. Borhani, J. Ceram. Process. Res. 16 (2015) 308-312.
- M. Demirel, and B. Aksakal, J. Ceram. Process. Res. 19 (2018) 5-10.
- 8. M. Ensoylu, A.M. Deliormanlı, and H. Atmaca, Biomimetics 8 (2022) 10.
- A.K. Gain, Y. Cui, L. Zhang, and Z. Li, Mater. Sci. Eng. A 911 (2024) 146961.
- 10. J.-H. Lee, and H.-K. Park, J. Ceram. Process. Res. 22 (2021) 590-596.
- M. Akmal, A. Malik, W. Jeong, and H.J. Ryu, Mater. Chem. Phys. 315 (2024) 129037.
- 12. J. Park, A.B. Tesler, E. Gongadze, A. Iglič, P. Schmuki,

- and A. Mazare, ACS Appl. Mater. Interfaces 16 (2024) 4430-4438.
- T. Kokubo, and H. Takadama, Biomaterials 27 (2006) 2907-2915.
- H. Jinyun, W. Weimin, F. Zhengyi, and S. Hui, J. Wuhan Univ. Technol. Mater. Sci. Ed. 20 (2005) 90-93.
- N.J. Henson, in, Rutgers The State University of New Jersey, School of Graduate Studies, 2023.
- F. Wang, G. Long, and J.L. Zhou, J. Hazard. Mater. 465 (2024) 133419.
- 17. Y. Qi, F. Zhang, B. Fan, X. Li, M. Chen, R. Zhang, H. Li, and Y. Chen, Ceram. Int. 50 (2024) 39235-39242.
- H. Ding, G. Zhou, T. Liu, M. Xia, and X. Wang, Tribol. Int. 89 (2015) 62-66.
- S. Hayakawa, In vitro degradation behavior of hydroxyapatite, in: Hydroxyapatite (HAp) for Biomedical Applications, Elsevier, 2015, pp. 85-105.
- 20. K.B. Narayanan, Biomimetics 10 (2025) 317.
- K. Soysal, J. Park, S. You, D. Shin, W. Bae, and A. Ozturk, J. Ceram. Process. Res. 12 (2011) 176-182.

- Z.-b. Guo, and F.-b. Kong, Trans. Indian Inst. Met. 78 (2025) 1-8.
- N. Wu, F. Xue, H. Yang, G. Li, and F. Luo, J. Ruan, Ceram. Int. 45 (2019) 1370-1378.
- S. Dudley, R. Avci, W. Gleason, W. Hill, J. Howery, M. Jaqua, and D. Margrave, J. Miner. Mater. Charact. Eng. 6 (2017) 72-85.
- 25. J.J. De Yoreo, and P.G. Vekilov, Rev. Mineral. Geochem. 54 (2003) 57-93.
- J.A. Rincón-López, J.A. Hermann-Muñoz, N.r. Cinca-Luis,
 L. López-Conesa, D.A. Fernández-Benavides, I. García-Cano,
 J.M. Guilemany-Casadamon,
 A.R. Boccaccini,
 J. Muñoz-Saldaña,
 and J.M. Alvarado-Orozco,
 Cryst. Growth Des. 20 (2020) 4030-4045.
- D.V. Abere, S.A. Ojo, G.M. Oyatogun, M.B. Paredes-Epinosa, M.C.D. Niluxsshun, and A. Hakami, Biomed. Eng. Adv. 4 (2022) 100056.
- A. Ebrahimi, H. Esfahani, O. Imantalab, and A. Fattah-Alhosseini, Trans. Nonferrous Met. Soc. China 30 (2020) 944-957.